Manuscript Details

Manuscript number	ETFS_2019_1055
Title	POOL BOILING HEAT TRANSFER OF HFE-7100 ON METAL FOAMS
Article type	Research Paper

Abstract

The search for new techniques to increase boiling heat transfer has been driven by more efficient and compact heat exchangers, especially in microelectronics and equipment with high thermal loads. Two-phase cooling systems are a promising thermal management technology for high-heat dissipation. In this context, the present study investigated the performance of modified heating surfaces consisting of metal foams of nickel (Ni) and copper (Cu). Pool boiling tests were performed using HFE-7100 as working fluid, at saturation conditions. The metal foams surfaces provided a higher heat transfer coefficient compared to plain surfaces and prevented thermal overshoot at the onset nucleate boiling. The Cu foam provided the best performance for the entire boiling curve. In general, for low and moderated heat fluxes, there is a combined effect of surface area and thermal conductivity of foams; the high surface area of Ni foam provides a barrier for the departure of the vapor bubble, inhibiting the cooling effect of the heating surface. For the Cu foam, no significant vapor trapped effect was observed, and the highest heat transfer coefficient was 12.4 kW/m²·K for a heat flux around 270 kW/m²; in addition, the thermal behavior is a function of the permeability and wickabillity behaviors of the surfaces.

Keywords	Pool boiling; metal foams; heat transfer coefficient; critical heat flux; foam thermal conductivity; pore diameter

Corresponding Author	Elaine Maria Cardoso
Corresponding Author's Institution	UNESP - Universidade Estadual Paulista
Order of Authors	Leonardo Lachi Manetti, Gherhardt Ribatski, Reinaldo Rodrigues de Souza, Elaine Maria Cardoso

Suggested reviewers

Submission Files Included in this PDF

File Name [File Type]

Cover Letter.pdf [Cover Letter]

Highlights.pdf [Highlights]

Graphical Abstract.pdf [Graphical Abstract]

Manetti_et_al_ETFS_2019_Final.pdf [Manuscript File]

Author Declaration.pdf [Conflict of Interest]

To view all the submission files, including those not included in the PDF, click on the manuscript title on your EVISE Homepage, then click 'Download zip file'.

POOL BOILING HEAT TRANSFER OF HFE-7100 ON METAL FOAMS

Leonardo Lachi Manetti[1], Gherhardt Ribatski[2], Reinaldo Rodrigues de Souza[1] and Elaine Maria Cardoso[1]*

[1]*UNESP – São Paulo State University, School of Natural Sciences and Engineering , Post-Graduation Program in Mechanical Engineering, Av. Brasil, 56, 15385-000, Ilha Solteira, SP, Brazil*

[2]*Heat Transfer Research Group, Department of Mechanical Engineering, Escola de Engenharia de São Carlos (EESC), University of São Paulo (USP), Brazil*

*corresponding author: elaine.cardoso@unesp.br

Abstract

The search for new techniques to increase boiling heat transfer has been driven by more efficient and compact heat exchangers, especially in microelectronics and equipment with high thermal loads. Two-phase cooling systems are a promising thermal management technology for high-heat dissipation. In this context, the present study investigated the performance of modified heating surfaces consisting of metal foams of nickel (Ni) and copper (Cu). Pool boiling tests were performed using HFE-7100 as working fluid, at saturation conditions. The metal foams surfaces provided a higher heat transfer coefficient compared to plain surfaces and prevented thermal overshoot at the onset nucleate boiling. The Cu foam provided the best performance for the entire boiling curve. In general, for low and moderated heat fluxes, there is a combined effect of surface area and thermal conductivity of foams; the high surface area of Ni foam provides a barrier for the departure of the vapor bubble, inhibiting the cooling effect of the heating surface. For the Cu foam, no significant vapor trapped effect was observed, and the highest heat transfer coefficient was 12.4 kW/m²·K for a heat flux around 270 kW/m²; in addition, the thermal behavior is a function of the permeability and wickabillity behaviors of the surfaces.

Nomenclature

Alphabetic

a_{sf}	Area density	[m^2/m^3]
b	Exponent relative to roughness effects	
c_p	Specific heat capacity	[J/kg·K]

C_{sf}	Surface-fluid coefficient	[-]
D_d	Bubble departure diameter	[m]
d_f	Fiber diameter	[m]
dh	Liquid column variation	[m]
d_p	Pore diameter	[m]
F	Inertia coefficient	[-]
f_w	Heat surface material parameter	[-]
h	Heat transfer coefficient	[W/m^2·K]
k	Thermal conductivity	[W/m·K]
k_{foam}	Foam effective thermal conductivity	[W/m·K]
k_{Cu}	Copper thermal conductivity	[W/m·K]
k_{mat}	Foam material thermal conductivity	[W/m·K]
K	Permeability	[m^2]
L	Copper block distances	[m]
L_b	Characteristic length	[m]
L_c	Corrected fin/foam length	[m]
M	Molar mass	[kg/kmol]
m	Exponent of heat flux in Eq.(17); fin/foam efficiency coefficient in Eq.(19) and Eq.(20)	
$\dot{m}$	Mass flow rate	[kg/s]
n	Stephan exponent	[-]
P	Pressure	[Pa]
Pr	Prandtl number	[-]
p_r	Reduced pressure	[-]
$q''_{measured}$	Heat flux measured at the copper block	[W/m^2]
R_a	Average roughness	[µm]
R_p	Maximum peak height of surface roughness	[µm]
s	Gap size	[m]
S	Square cross section area	[m²]
$\dot{V}$	Wicked volume	[m^3]
T	Temperature	[K]
t	Time	[s]
u	Uncertainty	
u	Fluid velocity	[m/s]

Greek symbols

δ	Foam thickness	[m]
ΔT	Temperature difference	[K]
ε	Porosity	[-]
η_{fin}	Pin-fin efficiency	[-]
η_{foam}	Foam efficiency	[-]
θ	Static contact angle	[degree]
μ	Dynamic viscosity	[kg/m·s]
ρ	Density	[kg/m^3]
σ	Surface tension	[N/m]

Subscripts

1, 2, or 3	Thermocouples position
air	Air properties
atm	Atmospheric condition

l or liq	Liquid
s	Surface square cross section
sat	Saturated state
vap	Vapor
w	Surface wall

1. Introduction

Efficient thermal management solutions are crucial to maintaining new electronic devices within the operating temperature limits [1]. Thermal management systems based on phase change such as pool and flow boiling, jet impingement, and sprays cooling are promising solutions to attend such high power dissipation needs [2].

Pool boiling heat transfer with the cooling device contacting directly the coolant eliminates the contact resistance associated to a significant temperature jump between the heat sink and the cooled device. However, such solution demands fluids with low electric conductivity, *e.g.*, water cannot be used. In this way, the fluorochemical fluids as fluorocarbons (FC-72, FC-82) and hydrofluoroether (HFE-7100, HFE-7200, HFE-7300) become suitable solutions due to their dielectric and inert properties; moreover, they are stable, nonflammable, and non-reactive, *i.e.*, chemically compatible [3]. Besides, FC-72 and HFE-7100 present a low boiling point ($T_{sat} \approx 60$ °C at 1 atm) to maintain the electronic components at low operating temperatures, < 85 °C [4]. Additionally, the hydrofluoroether fluid, HFE-7100 for instance, possess superior environmental properties (ozone depleting potential, ODP = 0; global warming potential, $GWP_{100} = 320$) [5]. Finally, fluorochemical fluids are high wetting liquids, what suppress nucleate boiling and highlights the demand for engineered surfaces in order to keep high heat transfer rates.

In this context, several combinations of liquid-surface operating under pool boiling conditions were evaluated and are summarized in the broad literature review presented by Shojaeian and Kosar [6]. Among the techniques presented in this study, engineering the surface morphology was one of the methods commonly used to enhance the heat transfer coefficient (HTC) and the critical heat flux (CHF). Such goals can be achieved by coating the surface with metal foams (high porosity surfaces) in order to create a porous structure that allows fluid inflow to keep nucleation sites active and protrusions that enlarge the boiling surface area [7, 8].

El-Genk and Parker [9] investigated pool boiling of HFE-7100 on a graphite foam with porosity ε = 60%, under saturation conditions. At high heat fluxes, they observed

for the porous surface a reduction around 9 K of the wall superheating compared to the plain surface. In addition, the temperature wall overshoot at the incipient boiling was not observed. Xu et al. [10] used acetone as working fluid on copper foam ($\varepsilon \geq 88\%$) with three different porous densities (porous per inch, PPI): 30, 60, and 90. For all foams configurations, the wall temperature excursion at boiling incipience was negligible. The authors associated the HTC enhancement to the higher liquid contact area, higher density of active sites, and capillary-assist liquid flow towards foam cells. Yang et al. [11] used the same surfaces and experimental methodology of Xu et al. [10] for water as working fluid. Based on the results of both studies, Yang et al. [11] pointed out that the HTC enhancement on the metal foams depends on the balance between the liquid suction capability towards the porous structure and the vapor release resistance to the bulk liquid. Xu and Zhao [12] investigated saturated pool boiling heat transfer of deionized (DI) water on a copper foam surface with V-shape grooves. They reported that large foam thickness offers high surface areas, however creates considerable flow resistance to the bubble scape. In this sense, grooves in the foam structure could help the vapor bubbles escape. Recently, Zhou et al. [8] investigated copper foams (with 10, 50, and 110 PPI) with pore density gradient in their structure and using water with and without n-butanol solution at 6 wt.% as working fluid. According to their results, the metal foams increase the HTC performance due to the increase of porous density for both fluids tested. In addition, for high heat fluxes, the surface tension of the n-butanol solution within the porous matrix decreases due to the increase of its concentration. Therefore, the bubble departure diameter is also reduced, allowing the vapor bubbles release. In the other hand, for water without n-butanol solution the gradient structure seems to present less effect on the HTC enhancement due to the foam caging effect. Wong and Leong [7] printed a homogeneous metal foam structure by using Selective Laser Melting (SLM) in order to study the effect of porous diameter and foam thickness on pool boiling of FC-72. They concluded that porous structures increase the bubble nucleation site density due to the larger surface area and capillary-assisted liquid suction which improves liquid replenishment; however, a larger surface area corresponds to an increase in the form drag and, consequently, in the bubble evacuation resistance. The bubble evacuation resistance increases for higher heat fluxes, structure height and for smaller unit cell sizes. Doretti et al. [13] carried out tests for aluminum foams (ε = 92%), 10 mm thick and porous densities of 5, 10, and 40 PPI. The boiling curves for the surfaces covered with foam presented remarkably lower wall superheating compared to

the plain surface. Moreover, 10 PPI and 40 PPI foams exhibited the same behavior, which was slightly different from that for 5 PPI. In the case of 5 PPI and for the range of experimental conditions evaluated by them, the HTC increased continuously while for 10 PPI and 40 PPI the HTC increased according to an almost constant gradient until a heat flux of 500 kW/m². Then, for heat fluxes higher than this value, the gradient of the heat transfer coefficient is significantly reduced. At low heat fluxes, the vapor bubbles are small and can easily escape from the foam. As the heat flux increases, the bubbles size grow, experiencing larger flow resistance through the porous layer: the highest the PPI, the largest flow resistance.

In this paper, the results of an experimental investigation concerning pool boiling of HFE-7100 on metal foams of copper (Cu) and nickel (Ni) are presented. The present work aims to: (i) provide literature with new heat transfer data; (ii) understand the vapor bubble dynamics associated to the heat transfer performance based on simultaneous high-speed filming and heat transfer coefficient measurements; (iii) and provide new insights to the development of new heat transfer enhancement surfaces operating with fluorochemical fluids.

2. Foams parameters

The porous surfaces used in the present study were purchased from Nanoshel® in 500 × 500 mm^2 panels. They are open cell metal foam, with 3 mm thick, fabricated by using metal deposition in a cellular preform as detailed by Ashby et al. [14] and Bahart [15]. They were cut in 16 × 16 mm^2 panels by using a wire electrical discharge machining (wire-EDM).

Their porosity (ε) was evaluated by weighting seven samples with the same size in an analytical balance and comparing the foam weight with that of a solid sample with an equivalent volume (16 × 16 × 3 mm³). Moreover, the following methods were used to characterize the metal foams: (i) optical images by using a stereo microscopy Zeiss® SteREO Discovery.V8 and scanning electron microscopy (SEM) by using an EVO LS15 Zeiss®, Tab. 1; (ii) microcomputer tomography (μCT) by using a Skycan 1272 at a resolution of 15 μm (100 kV X-ray source voltage); (iii) permeability based on air flow through the foam; and (iv) wickability based the wicked volume in a capillary tube (1 mm diameter), Tab. 3. The implementation of these two last methods is described in items 2.1 and 2.2, respectively.

Table 1. Metal foams Stereo and SEM images.

Material	Stereo (top view)	SEM (top view)	SEM (fiber cross section)
Cu	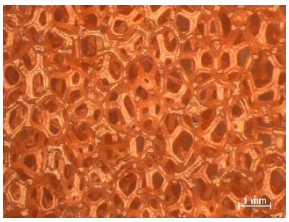	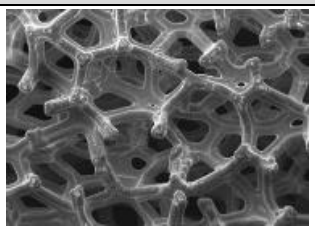	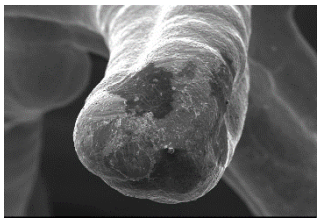
Ni	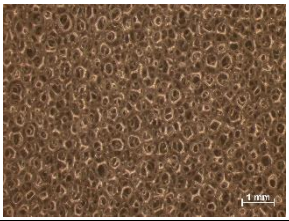	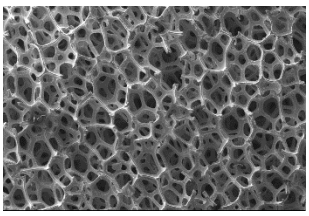	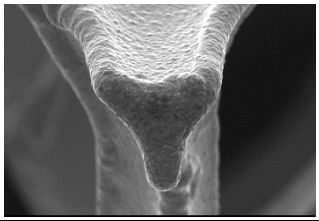

The numbers of pores per inch (PPI) also is a parameter that influences the heat transfer. This parameter was measured as proposed by Athreya et al. [16] and Zhu et al. [17]. In order to perform the PPI measurements by using the Stereo images, seven lines in each direction – horizontal and vertical, were traced and the number of porous intercepted by the lines was counted; so, an average yields the PPI of the open cell metal foam. For Cu and Ni open cell metal foam, the average PPI values were 31.75 and 62.72, respectively. Moreover, the µCT images were used for measuring the foam porous diameter and fibers diameters (d_p and d_f, respectively), and area density (a_{sf}). First, the µCT virtual slices were input in the Imoph software [18] in order to measure the surface granulometry by using the aperture map of both phases (solid and porous) as explained by Vicente et al. [19]. Figure 1 shows the histogram and the normal distribution that allows defining a mean pore diameter for each foam sample. Next, the µCT virtual slices were input in the vmtk® software to measure the area density. vmtk® uses 'marching cubes' algorithm to extract interfaces between the porous and solid phases, creating a polygonal mesh surface (see Figure 2). In order to distinguish the two phases, a grayscale threshold value was selected such that the porosity of the reconstructed 3D volume matched with the measured foam porosity (Table 1) as explained by Sarangi et al. [20]. After setting the correct gray scale, the area density was obtained by the ratio between the surface solid area (foam area) and its total volume (solid volume + porous volume). The results of ε, d_p, d_f, with the respective standard deviation according to a confidence interval of 95%, and a_{sf} are given in Table 2.

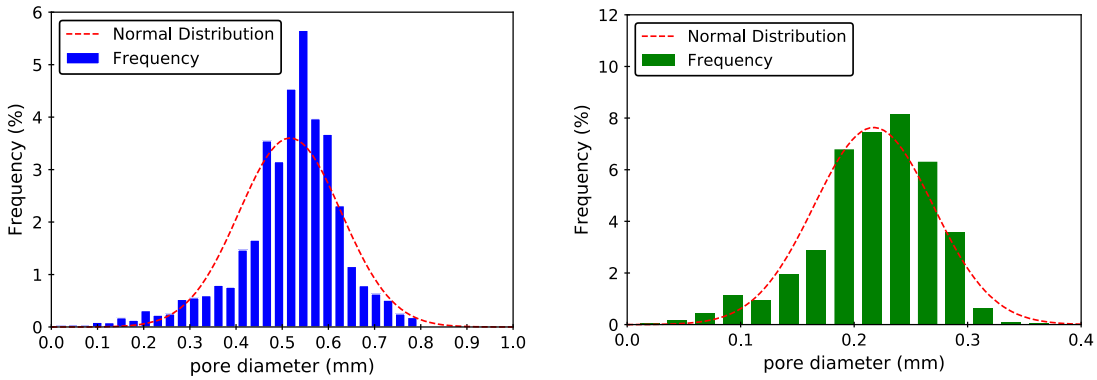

(a) (b)

Figure 1. Pore diameter distribution: (a) Cu foam; (b) Ni foam.

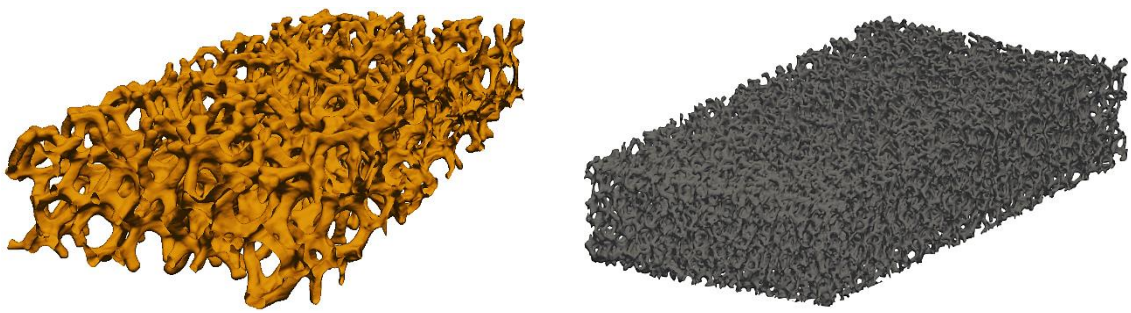

(a) (b)

Figure 2. Rendered tridimensional surfaces: (a) Cu foam; (b) Ni foam.

Table 2. Metals foams characteristics.

Material	Weight ($kg \times 10^{-3}$)	Foam density (kg/m^3)	Relative density[1](%)	ε (%)	d_p (mm)	d_f (mm)	a_{sf} (m^2/m^3)
Cu	0.697 ± 0.022	908.1 ± 28.63	10.0 ± 0.32	90.0 ± 0.32	0.52 ± 0.22	0.09 ± 0.04	2166
Ni	0.106 ± 0.010	138.0 ± 14.12	1.6 ± 0.15	98.4 ± 0.15	0.22 ± 0.10	0.04 ± 0.02	5133

[1]Pure material density: ρ_{Cu} = 8960 kg/m³; ρ_{Ni} = 8900 kg/m³ [21].

2.1 Foams permeability

The permeability (K) is a foam characteristic associated to the capacity of flow conductance through a porous media and is expressed in m^2. According to Macin et al. [22] the foam permeability can be obtained from Forchheimer–Darcy equation, re-written in this text as follows:

$$-\frac{dP}{dz}\cdot\frac{1}{u} = \frac{\rho_{air}F}{\sqrt{K}}u + \frac{\mu_{air}}{K} = a\cdot u + b \tag{1}$$

where u is the fluid velocity at the inlet of the foam (based on the cross section of the empty structure, S),

$$u = \frac{\dot{m}_{air}}{\rho_{air} \cdot S} \tag{2}$$

and F is the dimensionless inertia coefficient. Moreover, μ_{air} is the air dynamic viscosity and, ρ_{air}, the air density (both have been evaluated at the inlet). The air density was calculated by using the equation of state for an ideal gas - by considering the values of the pressure and temperature in the upstream flow - while the air dynamic viscosity was calculated by using the equation used by Gasche et al. [23], as follows,

$$\mu_{air} = (0.872 + 7.029 \times 10^{-2} \cdot T - 3.81 \times 10^{-5} \cdot T^2) \times 10^{-6} \tag{3}$$

In the present study, as presented by Macin et al. [22], the test facility schematically illustrated in Fig. 3 was built in order to evaluate the variation of the pressure drop gradient with the air flow velocity, and, then, from the curve given by Eq. (1), to extract the foams permeability.

The experimental tests were carried out using air from a reservoir containing compressed air at 9 bar. The mass flow rate was controlled by a needle valve and measured through a Coriolis mass flow meter (Rheonik RHM 04) with operating range of 5.0 kg/min and maximum uncertainty equal to ± 0.2% of the reading. A differential transducer with a measurement range from 0 to 0.1 bar (error of 0.1% of the full scale, FS) was used to measure the pressure drop across the foam surface. A barometer with 0.05 kPa resolution measured the atmospheric pressure. The upstream pressure was evaluated by gauge pressure transducer with 1 bar FS and uncertainty of ± 0.1% FS. A PT100 sensor (as part of the Coriolis mass flow meter) measured the temperature of the flow [23]. Figure 4a and 4b show the variation of the pressure drop gradient and the product of the pressure drop gradient and (1/u) with the air velocity.

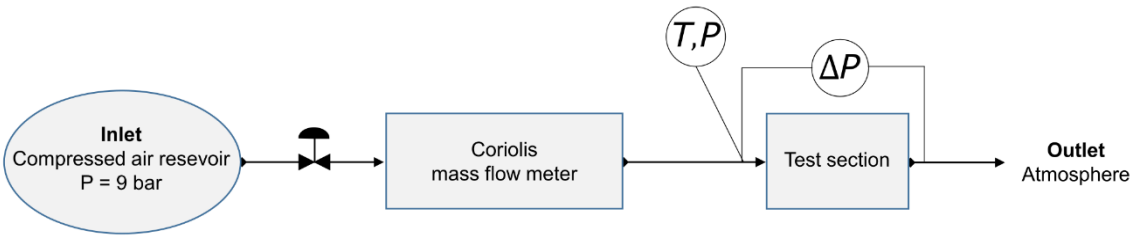

Figure 3. Layout of the experimental apparatus for permeability measurements.

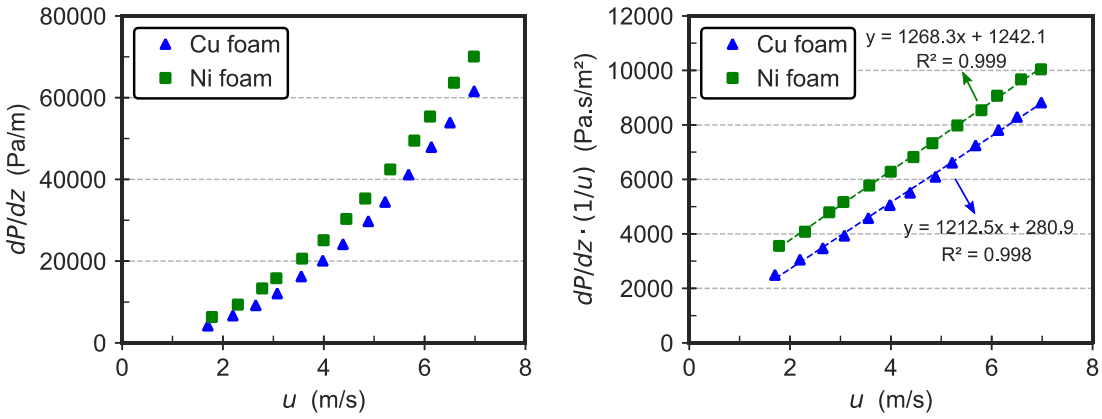

(a) (b)

Figure 4. Permeability tests: (a) Experimental pressure gradient and (b) Regression analysis.

From the linear curves (Fig. 4b) it was possible to calculate the permeability for both metal foams. It was obtained K equal to $0.66 \times 10^{-7} \pm 0.43 \times 10^{-7}$ m^2 and $0.15 \times 10^{-7} \pm 0.005 \times 10^{-7}$ m^2; and, F equal to 0.275 ± 0.091 and 0.136 ± 0.003 for Cu foam and Ni foam, respectively. As expected, the Cu foam presents a higher permeability due to the larger pore diameter than the Ni foam.

2.2 Metal foams capillary wicking

In the present study, the foam capillary wicking behavior was evaluated for HFE-7100 since authors [7, 10, 11, 13] associated the heat transfer enhancement provided by the foam to capillary wicking effect. Ahn et al. [24], Rahman et al. [25], Cao et al. [26, 27] carried out capillary-wicking test where the porous surface is slowly raised to contact a pendant fluid droplet attached to a small diameter capillary tube. As the surface contacts the liquid droplet, the fluid is wicked into the porous structure and the volumetric flow rate is measured by monitoring the liquid meniscus in the tube.

The experimental layout is shown in Fig. 5 where the capillary tube had 1 mm in diameter. The z-axis raised the surface up to it touches the tube while the high-speed camera recorded the meniscus displacement. After that, tracking image software was used to measure the liquid column variation inside the capillary tube and, then, the volume wicked was calculated. Table 3 shows the volume wicked by the surface at the first 50 milliseconds.

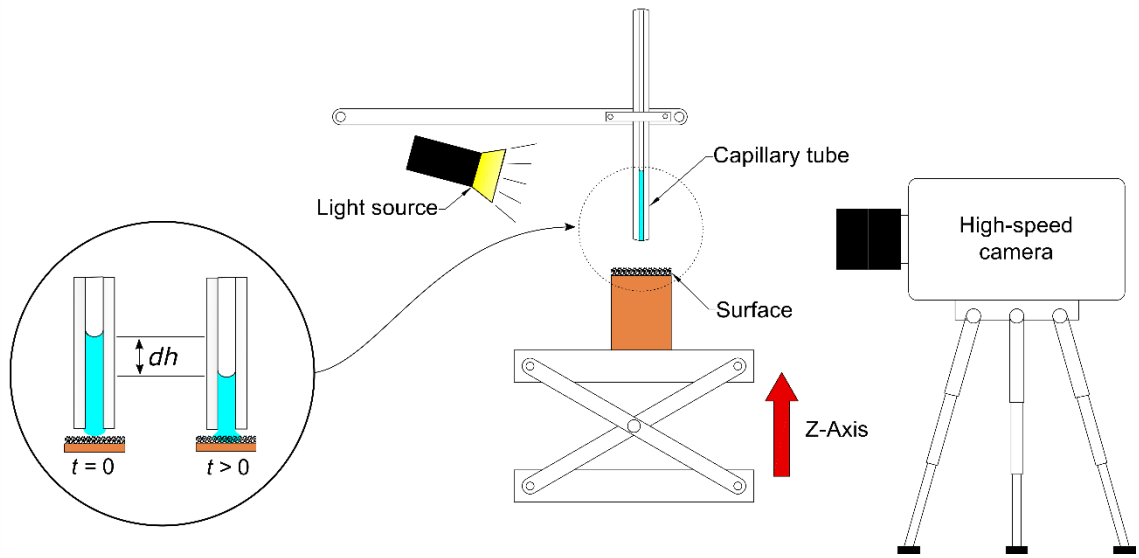

Figure 5. Schematic of the experimental device used for the wickability measurements.

One may observe that the Cu foam showed the best capillary wicking behavior with a total volume of 1.4 µL absorbed during the first 50 miliseconds while the Ni foam absorbed 0.84 µL. The plain surface showed the worst wicking result of 0.51 µL. According to Xu et al. [10], foams with small pore size present a large capability of pumping liquid due to their higher capillary pressure ($2\sigma/d_p$). Thus, according to this hypothesis, it was expected a higher wickability for the Ni foam. However, the fact that the Ni foam presents a higher contact area with the liquid, increasing the flow friction, seems to explain the higher wickability of the Cu foam. Wu et al. [28] reported similar result, where surfaces with small pores could facilitate the liquid wicking, while the surface irregularities could inhibit the liquid spreading as compared to surfaces with a larger number of micro-pores and microstructures (which assists the liquid spreading and wicking).

Table 3. Metal foams capillary wicking.

Plain		
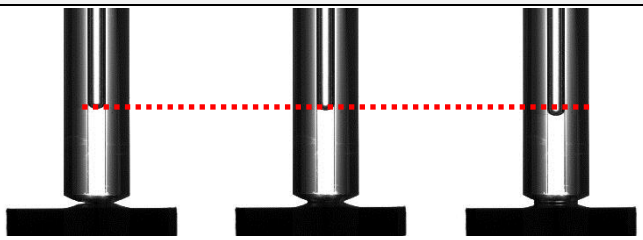		
0 ms	10 ms	50 ms

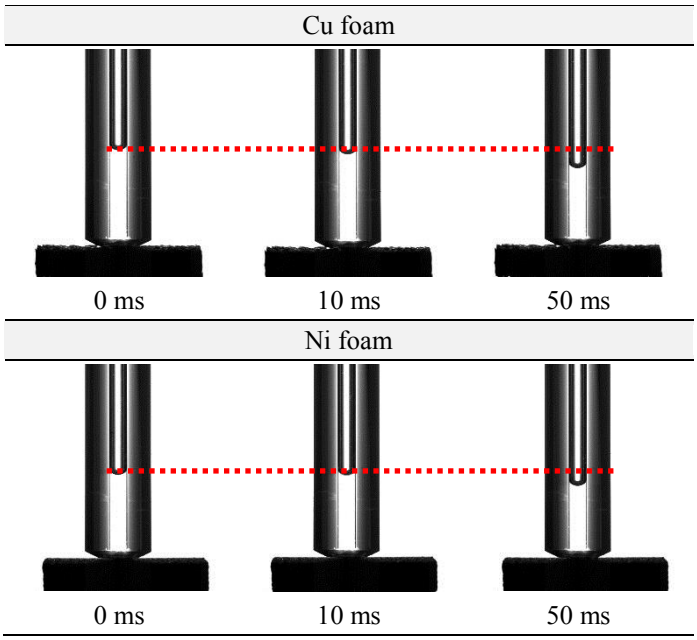

3. Experimental facility and data reduction

3.1 Experimental facility

The pool boiling tests were performed in the apparatus shown in Fig. 6, which consists of a rectangular vessel (120 × 100 x 200 mm^3) made of glass with wall thickness of 5 mm. The upper and lower bases consisted of two stainless steel plates, 200 × 200 × 10 mm³. The required tightness was obtained with nitrile rubber and silicone; additionally, screws were passed though the upper and bottom stainless steel plate in order to press the glass box against the nitrile rubber. Water from a thermal bath circulated through a cooling coil, located at the top of the boiling chamber. This heat exchanger was used to condensate the vapor generated by the heaters and to control the saturation pressure inside the vessel. An auxiliary heater – a cartridge resistance with a maximum power of 250 W at 220 V – submerged in the working fluid was used to maintain the liquid temperature near the saturation state. This heater was powered through a variable transformer. Two K-type thermocouples, T_{liq} and T_{vap}, located in the liquid and vapor regions of the vessel, respectively, were used to monitor the test fluid temperature. An absolute pressure transducer Omega PXM309-2A measured the pressure inside the boiling chamber. The experiments were performed under conditions close to the local atmospheric pressure, p_{atm} = 98 kPa. The pressure uncertainty, according to the calibration curve, is ± 0.05 kPa.

The test section, illustrated in Fig. 7, consisted of a copper piece with a square plate on the upper surface (16 × 16 × 3 mm^3) of the copper cylinder. The test section was machined from a unique copper piece in order to avoid thermal contact resistances among its components. Three K-type thermocouples (T_1, T_2, and T_3) with hot junction diameters of 0.5 mm were embedded within the cylinder. The thermocouple junctions were fixed at the center axis at the end of radial holes (1 mm diameter), machined in the cylinder. After positioning the thermocouple in the cylinder, the holes were filled with copper powder in order to ensure low contact resistance and avoid empty spaces, which could affect the temperature field in the copper piece. This cylinder is fixed on a second copper block containing a heater cartridge with a maximum power of 300 W at 220 V responsible for heating the test section. This resistance is powered by a variable DC power source. The test section was thermally insulated from the environment by a radial polytetrafluoroethylene (PTFE) layer with 30 mm thick.

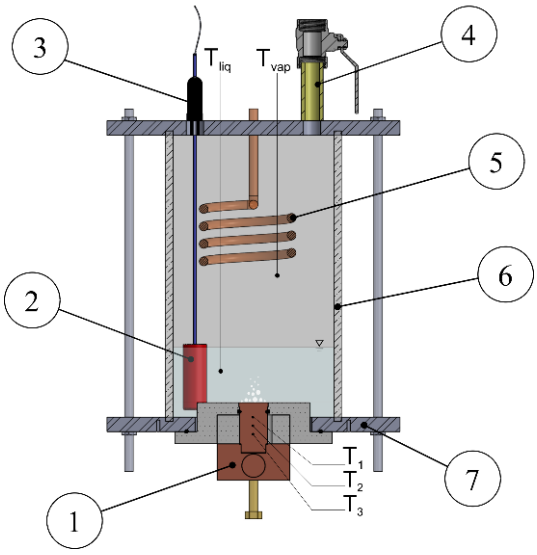

Figure 6. Pool boiling apparatus: (1) cooper block; (2) auxiliary heater; (3) pressure transducer; (4) vacuum/feed valve; (5) cooling coil; (6) glass chamber; (7) stainless steel plate.

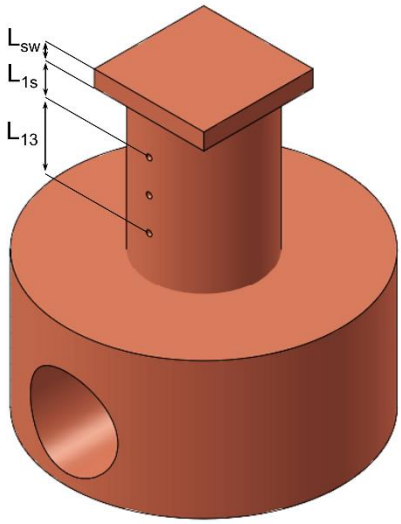

Figure 7. Distance between the thermocouples and the surface in contact with the working fluid.

The tests were performed using HFE-7100 (3M^{TM} Novec^{TM}) as working fluid at a saturation pressure of 98 ± 1 kPa. Results for a plain surface (R_a = 0.14 µm, Fig. 8a) polished according to procedure presented by Manetti et al. [29] was used as reference. To prevent the natural parasite sites at the interface between the PTFE piece and the test section surface, two-component epoxy resin was used to fill the gap as shown in Fig. 8a. The metal foams with a thickness (δ) of 3 mm (Figs. 8b and c) were welded on the copper block using tin-lead (0.1 mm thick) as solder, in order to ensure a low thermal resistance between the foam and the test section.

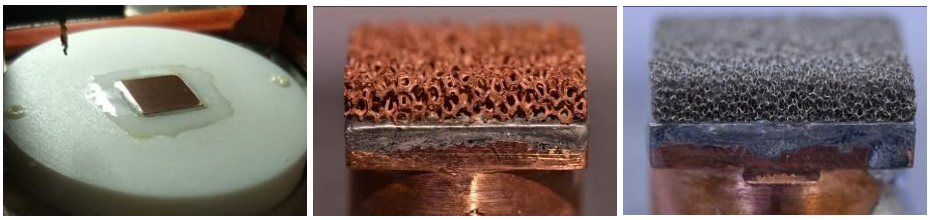

(a) (b) (b)

Figure 8. Heating surfaces: (a) plain; (b) Cu foam; and (c) Ni foam.

Before charging the vessel with the HFE-7100, the boiling chamber was evacuated until an absolute pressure of 10 kPa. Then, the chamber was feed with the working fluid. Before each series of tests, to eliminate non-condensable gases dissolved in the refrigerant, the auxiliary heater was powered and the working fluid boiled during a period of one hour.

The test conditions were adjusted by monitoring the pressure and the temperature inside the boiling chamber. For each metal foam test, the experiment was carried out at least twice under similar conditions to ensure that the results were repeatable.

A data acquisition system (Agilent 34970A) was used to acquire all the data signals (power, pressure, and temperature) and, then, they were registered in a personal computer using the Agilent Benchlink Data Logger.

The heating effect was imposed by increasing the electrical power according to heat flux steps of 10 kW/m² until a condition close to the CHF corresponding to a maximum footprint heat flux of 375 kW/m². Data were recorded for each heat flux step after the establishment of steady state conditions, characterized by variations in the measured temperatures within the uncertainty of their measurements (± 0.3 °C). At least 100 data points were recorded, corresponding to 500 seconds of steady state.

3.2 Data regression procedure and uncertainties estimation

Figure 9 shows the temperature profiles along the copper cylinder central axis based on the measurements of the thermocouples T1, T2 and T3 for different heat fluxes. According to this figure, linear curves fitting with R-square higher than 0.99 are obtained. Therefore, the assumption of negligible heat losses in the radial direction seems reasonable, as previously reported by Wu et al. [28] and Kiyomura et al. [30].

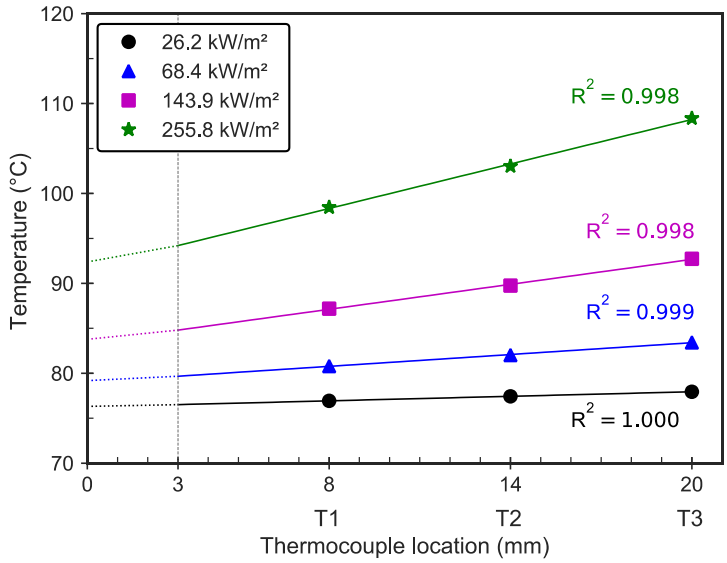

Figure 9. Verification of the one-dimensional Fourier law at the circular cross section (solid lines) and linear temperature profiles used to estimate the wall temperatures at the square cross section (dotted lines).

Thus, the heat flux was estimated based on the Fourrier law considering the thermocouples T1 to T3 as follows:

$$q''_{measured} = \frac{\pi}{4} \cdot k_{Cu} \cdot \frac{\Delta T_{13}}{L_{13}} \tag{4}$$

where L_{13} and ΔT_{13} are the distance from the thermocouples 1 to 3 and the temperature difference between them equal to 12 mm, as shown in Fig. 7.

The HTC was calculated by using the Newton's law of cooling given by:

$$h = \frac{q''_{measured}}{T_w - T_{sat}\,(p_{int})} = \frac{q''_{measured}}{\Delta T_{sat}} \tag{5}$$

where $T_{sat}(p_{int})$ corresponds to the saturation temperature of the HFE-7100 at the pressure inside de boiling chamber estimated as follows [5]:

$$\ln P_{sat}(\text{at Pascal}) = -\frac{3641.9}{T_{sat}(\text{at Kelvin})} + 22.415 \tag{6}$$

and T_w is the surface wall temperature also estimated according to Fourier's law and given as follows:

$$T_w = T_1 - \frac{q''_{measured}}{k_{Cu}} \cdot \frac{4}{\pi} L_{1s} - \frac{q''_{measured}}{k_{Cu}} \cdot L_{sw} \tag{7}$$

where the second term in the right-hand side is associated to the linear temperature profile at the end of circular section (L_{1s} = 5 mm) and the third term is associated to the linear temperature profile along the square section (L_{sw} = 3 mm) as shown Fig. 7.

The experimental uncertainties (u) were calculated by using the method described by Moffat [31] where the uncertainty in the result R is a function of the independent variables X_i as follow:

$$u_R = \left[\left(\sum_i^n \frac{\partial R}{\partial X_i} u_{X_i}\right)^2\right]^{\frac{1}{2}} \tag{8}$$

Therefore, the relative uncertainty for the heat flux between the thermocouples 3 and 1 was given by:

$$\frac{u_{q''_{measured}}}{q''_{measured}} = \left[\left(\frac{u_{\Delta T_{13}}}{\Delta T_{13}}\right)^2 + \left(\frac{u_{L_{13}}}{L_{13}}\right)^2\right]^{1/2} \tag{9}$$

where the uncertainty of the K-type thermocouples was ± 0.3 °C (corresponds to the thermocouples uncertainties after the calibration); the uncertainty of the thermocouple junction position was ± 0.03 mm, and the wall superheating uncertainty was given by:

$$u_{\Delta T_{sat}} = \left[u^2_{T_1 - T_{sat}} + \left(\frac{-(4/\pi)\cdot L_{1s} - L_{sw}}{k_{Cu}} u_{q''_{measured}}\right)^2 + \left(\frac{-(4/\pi)\cdot q''_{measured}}{k_{Cu}} u_{L_{1s}}\right)^2 + \left(\frac{q''_{measured}}{k_{Cu}} u_{L_{sw}}\right)^2\right]^{1/2} \tag{10}$$

Finally, the HTC uncertainty was given by:

$$\frac{u_h}{h} = \left[\left(\frac{u_{\Delta T_{sat}}}{\Delta T_{sat}}\right)^2 + \left(\frac{u_{q''_{measured}}}{q''_{measured}}\right)^2\right]^{1/2} \tag{11}$$

Therefore, the experimental uncertainty of the heat transfer coefficient is higher for low heat fluxes, decreasing as heat fluxes increase. For all surfaces tested, the experimental uncertainty for the heat flux and the heat transfer coefficient varied from 18.3% to 3.3% and from 18.4% to 3.8%, respectively.

4. Results and Discussion

4.1 Validation of the experimental apparatus

In order to check the accuracy of the pool boiling apparatus and the data regression procedure, tests were carried out for HFE-7100 on the plain surface, comparing them with predictions values based on well-known correlations from the literature (Fig. 10). The re-written version of the Rohsenow's correlation [32] is given:

$$h = \frac{1}{C_{sf} Pr_l^{1,7}} \frac{q'' c_{pl}}{h_{lv}} \left[\frac{\mu_l h_{lv}}{q''} \sqrt{\frac{g(\rho_l - \rho_v)}{\sigma}}\right]^{1/3} \tag{12}$$

where μ_l, h_{lv}, c_{pl}, and Pr_l are the liquid dynamic viscosity (kg/m·s), the latent heat of vaporization (J/kg), the liquid specific heat (J/kg·K), and the Prandtl number of the

liquid, respectively. In addition, σ is the surface tension, ρ_l and ρ_v are the liquid and vapor densities, respectively, and g is the gravitational acceleration. C_{sf} is a coefficient that depends on the fluid and the heating surface material. The thermophysical properties of the HFE-7100 were obtained from 3M Company [5] and Raush et al. [33] at p_{sat} = 98 kPa.

The correlation of Kiyomura et al. [34] is given by:

$$\frac{hL_b}{k_l} = 154\left[\left(\frac{c_{pl}T_{sat}}{h_{lv}}\right)^{1,72}\left(\frac{c_{pl}\mu_l}{k_l}\right)^{-0,34}\left(\frac{D_d q''}{\mu_l h_{lv}}\right)^{0,62}\left(\frac{s}{L_b}\right)^{-0,05}\right] \tag{13}$$

where D_d is the bubble departure diameter calculated as suggested by Fritz [35]:

$$D_d = 0.0208 \cdot \theta \cdot L_b \tag{14}$$

and L_b is the characteristic length given by $L_b = \sqrt{\frac{\sigma}{g(\rho_l - \rho_v)}}$; k_l is the fluid thermal conductivity. The parameter s is the gap size for confined boiling. In the present study it was considered the liquid column above the heating surface (s = 50 mm) since the boiling process did not occur under confined conditions.

Cooper [36] proposed a correlation to predict the boiling heat transfer coefficient taking into account the surface roughness and reduced pressure of the liquid,

$$h = 55p_r^b(-\log p_r)^{-0.55}M^{-0.5}q''^{0.67} \tag{15}$$

where $b = (0.12 - 0.2\log R_p)$, and p_r, M and R_p represent the reduced pressure, the molar mass of the working fluid, and the maximum peak height of surface roughness, respectively. In the present study, the correlation was evaluated based on the average surface roughness, R_a, whereas Cooper's correlation includes the parameter, R_p. Thus, for the present analysis, the following expression suggested by Gorenflo [37] was used:

$$R_a = 0.4R_p \tag{16}$$

Likewise, Ribatski and Jabardo [38] proposed an empirical correlation to estimate the boiling heat transfer in terms of reduced pressure. Their correlation was based on the experimental data for saturated pool boiling of halocarbon refrigerants on cylindrical surfaces of different materials:

$$h = f_w p_r^{0.45}(-\log p_r)^{-0.8} M^{-0.5} R_a^{0.2} q''^m \quad (17)$$

where $m = 0.9 - 0.3p_r^{0.2}$ and f_w is the heat surface material parameter, equal 100 to copper.

Finally, the curve fitting proposed by Stephan [39] based on the relation between the heat transfer coefficient and the heat flux was considered:

$$h = Cq''^n \quad (18)$$

where C is a coefficient dependent on the surface-fluid interaction and reduced pressure, and n is an exponent of the heat flux.

The predicted values agree reasonably well with the experimental data providing a mean absolute percentage error (MAPE) of 11% for the prediction method of Rohsenow [32] using the value of $C_{sf} = 0.00316$ as proposed by Priarone [40]; and, 12% for Kiyomura et al. [34] correlation assuming an static contact angle, θ, of 2 degree, a value that seems reasonable considering the high wettability of the HFE-7100. Cooper's correlation [36] presents a MAPE of 26% and, Ribatski and Jabardo [38] correlation presents the lower error, equal to 10.6%. The exponent n obtained by fitting the curve h vs. q'' as proposed by Sthepan's was around 0.7, agreeing with the values from literature which generally lies between 0.6 and 0.8. It is worth mentioning that the last two points in Fig. 10 are close to the critical heat flux; thus, it is reasonable that the pool boiling prediction method does not capture the trend of the heat transfer coefficient under such condition.

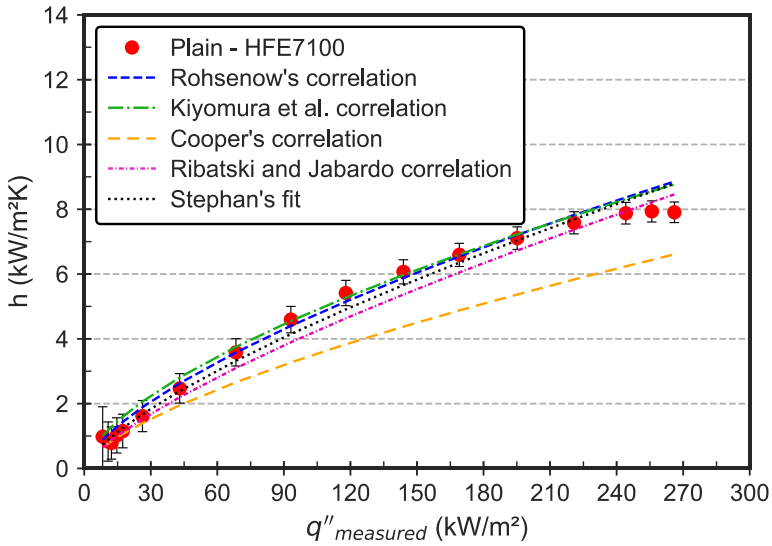

Figure 10. Pool boiling apparatus validation with HFE-7100.

4.2 Metal foams pool boiling curves

The metal foams boiling curves are shown in Fig. 11 and the corresponding curves displaying the HTC behaviors in Fig. 12. Both figures include the results for the plain surface. One may observe that both metal foams eliminated the thermal overshoot necessary to the onset of nucleate boiling (ONB). In fact, nucleation sites are already activated for the lowest evaluated heat flux (≈10 kW/m²) and superheating lower than 5 °C. For the plain surface, the sites remain non-actives until a heat flux of 15 kW/m² and superheating higher than 15 °C were attained. El-Genk and Parker [9] also detected it for graphite porous surface, attributing this phenomenon to the entrapped air in the high volume interconnected porosity and the re-entrant cavities in the surface. Additionally, Wong and Leong [7] reported that lower boiling incipience superheat is due to the larger surface area and more active nucleation sites (due to the porous structure). According to them [7], the incipience nucleation is highly sensitive to the nucleation sites available on the surface. For the porous structure, the intersections of struts form cavities, which can be suitable for nucleation, thus allowing lower boiling incipience superheat as compared to the plain surface. Xu et al. [10] also reported that miniature bubbles nucleate at the foam ligaments and fiber junctions in foam cells.

For moderated heat fluxes (≈120 kW/m²), the HTC enhancement becomes evident by a decrease in the wall superheating of 11.4 K for Cu foam and 12.1 K for Ni foam, as compared to the plain surface for a similar heat flux. This result implies a HTC augmentation of 100% and 82% promoted by the Cu and Ni foams, respectively. For heat flux values higher than 120 kW/m², the vapor within the Ni foam structure began to create an unstable boiling pattern, probably promoting intermittent dry patches within the foam structure, which increases the wall temperature and, consequently, degrades the heat transfer coefficient. For high heat fluxes (≈200 kW/m²), the wall superheating for Cu and Ni foams are about 16.6 K and 22.5 K, respectively. For the Ni foam, the HTC decreases for heat fluxes higher than 125 kW/m², indicating the occurrence of the dryout phenomenon associated to the vapor captured by the foam structure, which inhibits the liquid replenishment effect, degrading the heat transfer coefficient (Fig. 12). In addition, Wong and Leong [7] noted that the smaller the pore cell, the higher is the bubble evacuation resistance. This causes a large liquid-vapor counter-flow since the liquid replenishment is inhibited, leading to a lower heat transfer coefficient and an earlier occurrence of CHF.

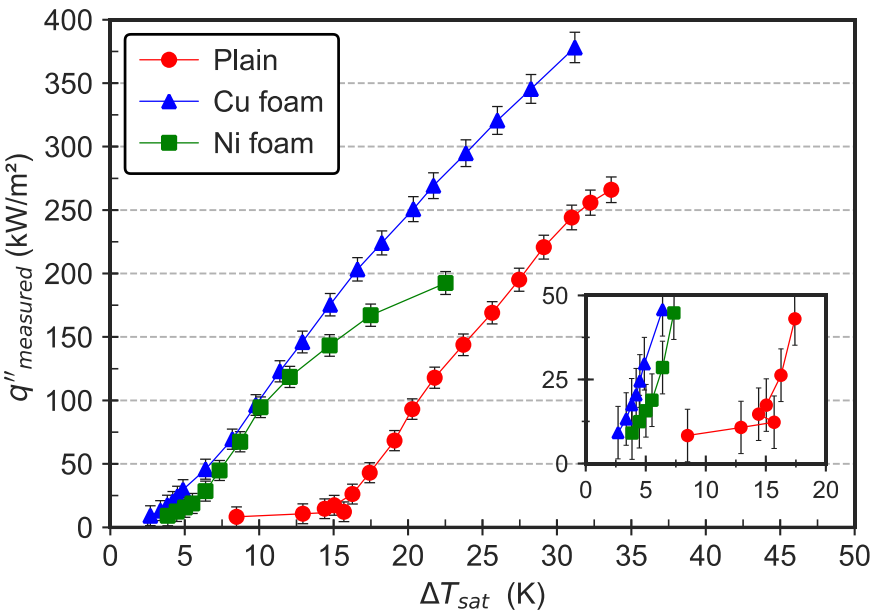

Figure 11. HFE-7100 pool boiling curves at saturation temperature.

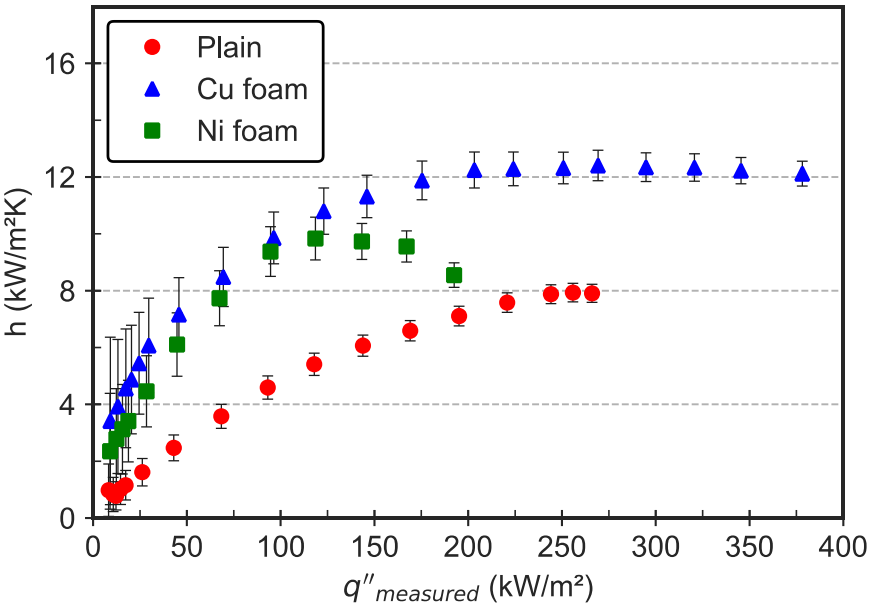

Figure 12. HTC performance for HFE-7100 on plain and metal foam surfaces.

As showed in Table 2 (section 2), smaller pore diameters and higher PPI implies on increasing the surface area density. Hence, it can be concluded that the Ni foam presents a higher contact area between its effective surface and the fluid than the Cu foam, which should increase the HTC. However, the thermal conductivity of Cu is approximately 5 times higher than the Ni thermal conductivity; in addition, the metal foam thermal conductivity is different from the solid material one, due to the porous medium. Thus,

the metal foams thermal conductivity was calculated by using the model of Calmidi and Mahajan [41] that considers the porous medium formed by two-dimensional array of hexagonal cells. The model yields a $k_{Cu;foam}$ = 13.27 W/m·K and $k_{Ni;foam}$ = 0.83 W/m·K, corresponding to a Cu foam thermal conductivity 16 times higher. In order to understand the metal foam thermal conductivity values in the foam temperature distribution, it was considered the metal foam fiber as a pin-fin with diameter equal to d_f and length equal to δ. Hence, it was used the fin efficiency equation,

$$\eta_{fin} = \frac{\tanh mL_c}{mL_c} \tag{19}$$

where $m = \left(4h/k_{foam}d_f\right)^{1/2}$ and $L_c = \delta + (d_f/4)$. By considering a HTC value of 10 kW/m²·K, the efficiency was equal to 5.7% and 0.1% for Cu foam and Ni foam, respectively. Despite these considerations, the Cu foam presented an order of magnitude higher than the Ni foam.

Mancin et al. [42] proposed a model for foam surfaces efficiency based on their data regression:

$$\eta_{foam} = \frac{1 + \frac{\tanh mL_c}{mL_c} \cdot a_{sf} \cdot \delta}{1 + a_{sf} \cdot \delta} \tag{20}$$

where,

$$m = \left(\frac{4 \cdot h}{d_f k_{mat}}\right)^{0.5} \cdot \left(\frac{k_{mat}}{k_{liq}}\right)^{0.52} \tag{21}$$

and

$$L_c = 1055 \cdot \delta^{1.18} \cdot \mathrm{PPI} \cdot \left(0.0254 - d_f \cdot \mathrm{PPI}\right)^{0.66} \tag{22}$$

From Mancin et al. [42] model, the foam efficiency was equal to 16.04% and 6.30% for Cu and Ni foams, respectively (as found out previously, the Cu foam presented an order of magnitude higher than the Ni foam). Therefore, the foam thermal conductivity plays an important role in the boiling heat transfer process.

For q'' > 120 kW/m², it is reasonable to infer that the vapor mass within the Ni foam structure increases the bubble evacuation resistance due to the larger heat transfer surface area, and consequently, the smaller area available for the vapor release.

Moreover, the bubble evacuation resistance is more pronounced as the heat flux and the foam height increase, as also pointed out by Wong and Leong [7].

For Cu foam, the highest HTC occurs at heat fluxes close to 270 kW/m². The maximum HTC for the Cu foam at a highest heat flux compared to the Ni foam is explained by the capillary-assisted behavior of the Cu foam, which improves liquid replenishment in the porous matrix delaying the dryout occurrence.

4.3 Vapor bubble dynamic visualization

Bubbles dynamics were visualized by using a high-speed camera (Photron FASTCAM SA3) with 1024 × 1024 maximum resolution at 1000 fps. Through videos and image tracking software, the bubble departure diameter (D_d) was calculated by averaging three diameter measurements of a spherical single-bubble immediately after its detachment from the surface, according to the procedure presented by Thiagarajan et al. [43]. For each heat flux, the bubble diameters were measured for at least three different bubble departure sites for a recording period of 1 second. Then, the arithmetic average diameters of all the evaluated bubbles for a certain experimental condition were calculated.

Figure 13 shows the results of the bubble departure diameter for five different walls superheating, corresponding to heat fluxes from 10 to 25 kW/m². In this figure, the error bars correspond to the standard deviations of the measured values. The coalescence of the vapor bubbles makes measurements above 25 kW/m² difficult and not reliable. According to Fig. 13, the procedure used to evaluate the bubble departure diameter is satisfactory because a reasonable agreement is found among the experimental results of the present study and those of Thiagarajan et al. [43], Borishanskiy et al. [44] and Phan et al. [45], for plain surfaces. It is worth mentioning that none of the prediction methods for bubble departure diameter considers surface morphology; however, Phan et al. [45] incorporates the influence of fluid properties and an energy factor as the contribution of the wetting effects, while Fritz [35] and Cole and Rohsenow [46] correlations only take into account a balance between buoyancy and surface tension forces, not being able to predict the HFE-7100 bubble departure diameter.

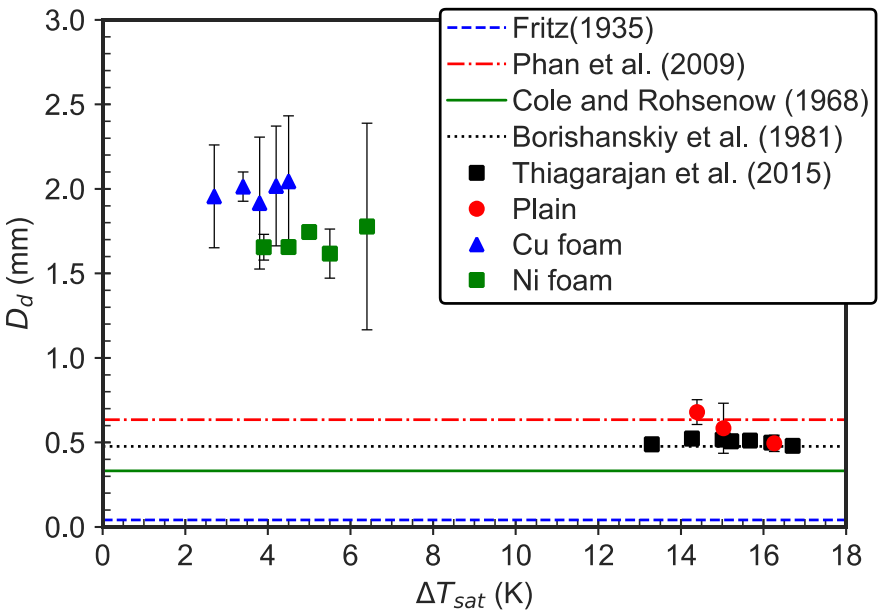

Figure 13. Bubble departure diameter distribution.

The vapor bubbles growing and coalescence within the foam structure lead to larger bubble departure diameters for the foam surfaces than for the plain surface, as the results displayed in Fig. 13 and the bubbles images shown in Fig. 14. These larger bubbles are similar to "cage bubbles" reported by Xu et al. [10]. From the analyses of Figs. 13 and 14, for low heat fluxes, the Cu foam provides larger bubbles departure diameter due to its larger porous diameters that allows bubbles to rise easily to the foam top. It is similar to the behavior reported by Sadaghiani et al. [47], who attribute the vapor bubbles size to the forces acting within the porous medium; the denser and smaller the pore sizes, the smaller the vapor bubbles and vice-versa.

According to Fig. 14, as the heat flux increases from 18 kW/m² to 45 kW/m², the bubbles departure diameter from the foam surface are still bigger, however a much higher density of bubble departure sites is noted on the plain surface. Further heat flux increases, up to the condition for which the HTC presents its maximum value, show that the bubbles flow not only through the foam upper surface but also through its lateral sides. This behavior is more pronounced for Ni foam due to its smallest pore diameter. The highest bubble evacuation resistance is due to the larger foam contact area with the fluid, increasing the flow friction and blocking the liquid-vapor counter-flow, decreasing the HTC. In fact, for the highest HTC values, vapor bubbles coalesce very quickly leading to an unstable boiling pattern, which causes an earlier dryout than when

the boiling pattern is stable at the same heat flux, as also reported by Wong and Leong [7].

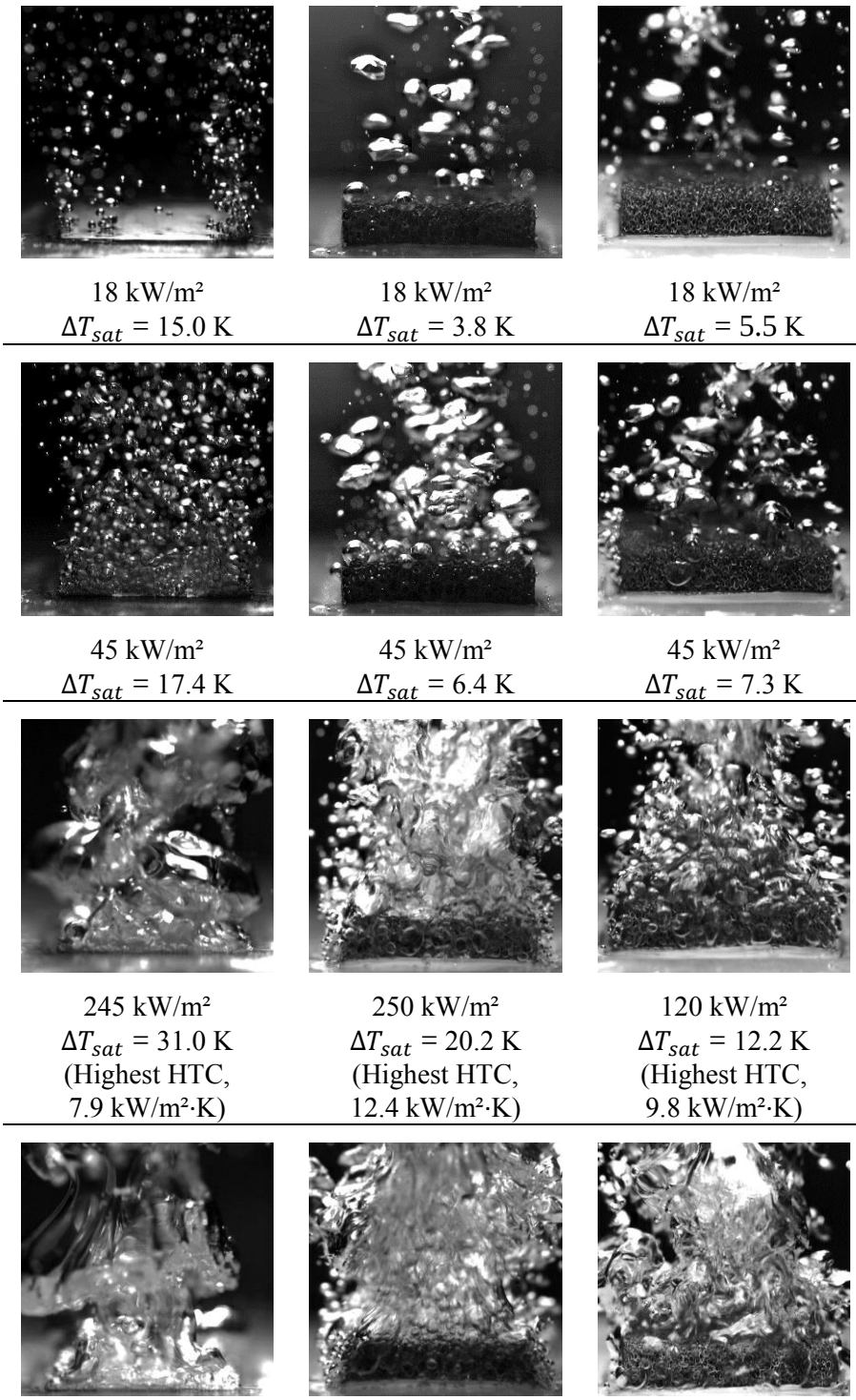

Plain	Cu foam	Ni foam
18 kW/m² ΔT_{sat} = 15.0 K	18 kW/m² ΔT_{sat} = 3.8 K	18 kW/m² ΔT_{sat} = 5.5 K
45 kW/m² ΔT_{sat} = 17.4 K	45 kW/m² ΔT_{sat} = 6.4 K	45 kW/m² ΔT_{sat} = 7.3 K
245 kW/m² ΔT_{sat} = 31.0 K (Highest HTC, 7.9 kW/m²·K)	250 kW/m² ΔT_{sat} = 20.2 K (Highest HTC, 12.4 kW/m²·K)	120 kW/m² ΔT_{sat} = 12.2 K (Highest HTC, 9.8 kW/m²·K)
266 kW/m² ΔT_{sat} = 33.6 K (Dryout heat flux)	375 kW/m² ΔT_{sat} = 31.2 K (Dryout heat flux)	200 kW/m² ΔT_{sat} = 22.5 K (Dryout heat flux)

Figure 14. Vapor bubbles pattern at different heat flux values.

4.4 Influence of foams parameters

In summary, the Cu foam shows better boiling performance for all heat fluxes than the Ni foam even the latter providing the highest effective surface area in contact to the fluid. By foams parameters analyses, Cu presents higher thermal conductivity than Ni; therefore, the thermal conductivity plays a key role in the boiling performance with foam surface due to the thermal gradient that occurs in the foam, such as a fin surface. Moreover, the porous surfaces present different pore diameters, which are linked to the area density (a_{sf}) and permeability (K). The smaller the pore diameter of an open-cell metal foam, the higher the area density, which improves the nucleate boiling and natural convection heat transfer; moreover, as the bubble nucleation strongly depends on the liquid superheat and presence of trapped gas, the intersections of foam fibers can form cavities with entrapped gas, which is suitable for nucleation, thus eliminating the ONB overshoot as compared to the plain surface. However, as the heat flux increases the number of active nucleation sites also increases, leading the vapor bubbles to stay trapped in the foam cell; the foam permeability also decreases with decreasing the foam pore diameter (the liquid cannot flows into the foam structure, deteriorating the HTC). Figure 15 summarize the effect of the foam parameters on pool boiling heat transfer.

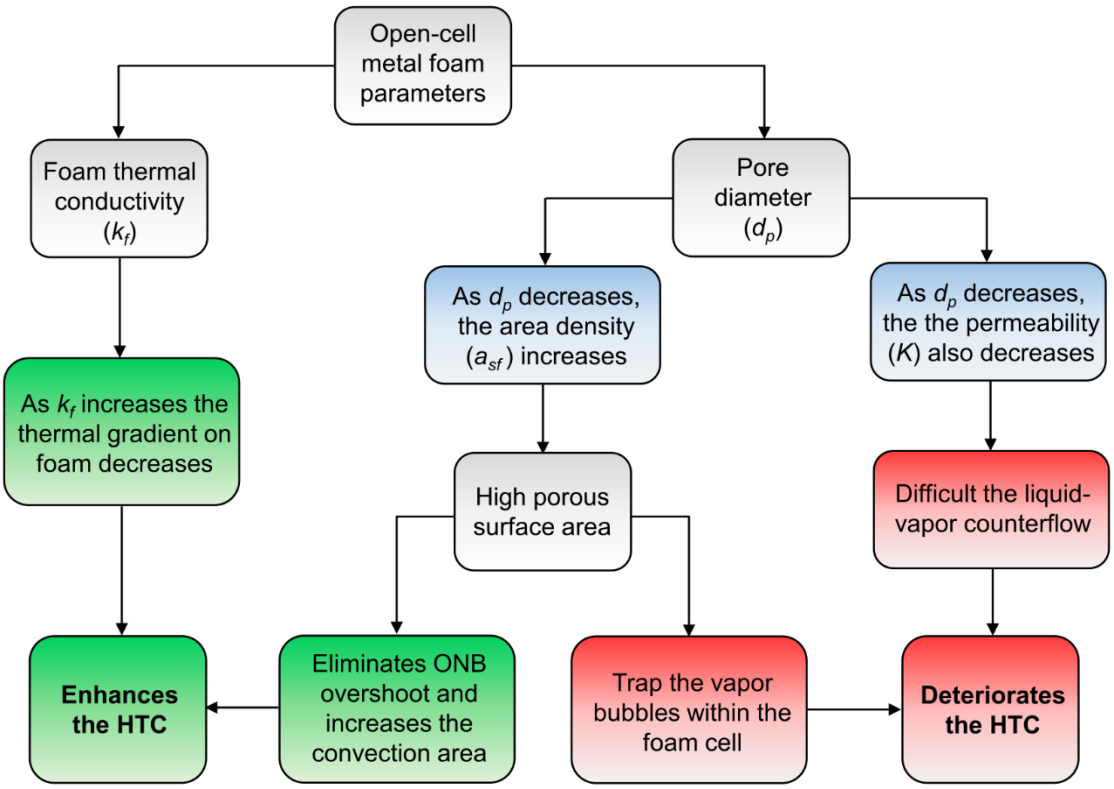

Figure 15. Effect of open-cell metal foam parameters on pool boiling performance.

5. Conclusions

In this work, we presented a pool boiling experimental work by using HFE-7100, at saturation conditions, and metal foams of copper (Cu) and nickel (Ni) as heating surfaces. The following conclusions can be drawn from the present study:

- The metal foams are able to absorb and spread the fluid more efficiently, being able to increase the HTC as compared to the plain surface. Moreover, these surfaces prevent thermal overshoot at the onset nucleate boiling.
- The metal foam thermal conductivity plays a key role in the boiling curve; Cu foam shows a better performance as compared to Ni foams, even with a smallest surface area.
- The high area density of Ni foam provides a barrier for the departure of the vapor bubble, inhibiting the cooling effect of the heating surface (incipience dryout occurs earlier).
- The capillary wicking of the copper foam contributed for the stable HTC at high heat fluxes.

It is worth mentioning that our recent studies are focused on the foams thickness in order to find the optimum foam thickness related to the foam pore diameter and thermal conductivity.

Acknowledgments

The authors are grateful for the financial support from the PPGEM – UNESP/FEIS, from CAPES, from the National Council of Technological and Scientific Development of Brazil (CNPq grant number 458702/2014-5) and from FAPESP (grant number 2013/15431-7; 2017/13813-0). We also extend our gratitude to Prof. Dr. Alessandro Roger Rodrigues, Prof. Dr. Tito José Bonagamba (Escola de Engenharia de São Carlos/EESC-USP) and Iago Lessa de Oliveira (UNESP/FEIS) for their important contribution to this work.

References

[1] K.C. Leong, J.Y. Ho, K.K. Wong, A critical review of pool and flow boiling heat transfer of dielectric fluids on enhanced surfaces, Appl. Therm. Eng. 112 (2017) 999–1019. doi:10.1016/j.applthermaleng.2016.10.138.

[2] M.S. El-Genk, Immersion cooling nucleate boiling of high power computer chips, Energy Convers. Manag. 53 (2012) 205–218. doi:10.1016/j.enconman.2011.08.008.

[3] G. Liang, I. Mudawar, Review of pool boiling enhancement by surface modification, Int. J. Heat Mass Transf. 128 (2019) 892–933. doi:10.1016/j.ijheatmasstransfer.2018.09.026.

[4] E. Teodori, A.S. Moita, A.L.N. MOREIRA, Empirical and modeling-based correlations for pool boiling on microstructured surfaces, Interfacial Phenom. Heat Transf. 2 (2014) 273–292. doi:10.1615/InterfacPhenomHeatTransfer.2015011663.

[5] 3M product brochure, 3M Novec™ engineered fluid HFE-7100 for heat transfer, (2002).

[6] M. Shojaeian, A. Koşar, Pool boiling and flow boiling on micro- and nanostructured surfaces, Exp. Therm. Fluid Sci. 63 (2015) 45–73. doi:10.1016/j.expthermflusci.2014.12.016.

[7] K.K. Wong, K.C. Leong, Saturated pool boiling enhancement using porous lattice structures produced by Selective Laser Melting, Int. J. Heat Mass Transf. 121 (2018) 46–63. doi:10.1016/j.ijheatmasstransfer.2017.12.148.

[8] L. Zhou, W. Li, T. Ma, X. Du, International Journal of Heat and Mass Transfer Experimental study on boiling heat transfer of a self-rewetting fluid on copper foams with pore-density gradient structures, Int. J. Heat Mass Transf. 124 (2018) 210–219. doi:10.1016/j.ijheatmasstransfer.2018.03.070.

[9] M.S. El-Genk, J.L. Parker, Enhanced boiling of HFE-7100 dielectric liquid on porous graphite, Energy Convers. Manag. 46 (2005) 2455–2481. doi:10.1016/j.enconman.2004.11.012.

[10] J. Xu, X. Ji, W. Zhang, G. Liu, Pool boiling heat transfer of ultra-light copper foam with open cells, Int. J. Multiph. Flow. 34 (2008) 1008–1022. doi:10.1016/j.ijmultiphaseflow.2008.05.003.

[11] Y. Yang, X. Ji, J. Xu, Pool boiling heat transfer on copper foam covers with water as working fluid, Int. J. Therm. Sci. 49 (2010) 1227–1237. doi:10.1016/j.ijthermalsci.2010.01.013.

[12] Z.G. Xu, C.Y. Zhao, Thickness effect on pool boiling heat transfer of trapezoid-shaped copper foam fins, Appl. Therm. Eng. 60 (2013) 359–370. doi:10.1016/j.applthermaleng.2013.07.013.

[13] L. Doretti, H. Sadafi, G. Righetti, K. Hooman, G.A. Longo, S. Mancin, Aluminum Foams for Water Pool Boiling Enhancement, (2019) 8075–8082. doi:10.1615/ihtc16.pma.022819.

[14] M. F. Ashby, T. Evans, N. A. Fleck, J. W. Hutchinson, H. N. G. Wadley, , L. J.. Gibson, Metal foams: a design guide. Elsevier, 2000.

[15] J. Banhart, Manufacture, characterization and application of cellular metals and metal foams, Prog. Mater. Sci. 46 (2001) 559–632. doi: 10.1016/S0079-6425(00)00002-5

[16] B. Athreya, R. Mahajan, S. Sett, Pool Boiling of FC-72 over Metal Foams: Effect of Foam Orientation and Geometry, In: 8th AIAA/ASME Jt. Thermophys. Heat Transf. Conf. (2002) 1–10. doi:10.2514/6.2002-3214.

[17] Y. Zhu, H. Hu, S. Sun, G. Ding, Heat transfer measurements and correlation of refrigerant flow boiling in tube filled with copper foam, Int. J. Refrig. 38 (2014) 215–226. doi:10.1016/j.ijrefrig.2013.04.012.

[18] Brun, E., Vicente, J., Topin, F., & Occelli, R., 2008. IMorph: A 3D morphological tool to fully analyse all kind of cellular materials. Cellular Metals for Structural and Functional Applications.

[19] J. Vicente, F. Topin, J.-V. Daurelle, Open Celled Material Structural Properties Measurement: From Morphology To Transport Properties, Mater. Trans. 47 (2006) 2195–2202. doi:10.2320/matertrans.47.2195.

[20] S. Sarangi, J.A. Weibel, S. V. Garimella, Quantitative Evaluation of the Dependence of Pool Boiling Heat Transfer Enhancement on Sintered Particle Coating Characteristics, J. Heat Transfer. 139 (2016) 021502. doi:10.1115/1.4034901.

[21] MatWeb, LLC. MatWeb, Material Property Data. http://www.matweb.com/

[22] S. Mancin, C. Zilio, A. Cavallini, L. Rossetto, International Journal of Heat and Mass Transfer Pressure drop during air flow in aluminum foams, Int. J. Heat Mass Transf. 53 (2010) 3121–3130. doi:10.1016/j.ijheatmasstransfer.2010.03.015.

[23] J.L. Gasche, D.M. Arantes, T. Andreotti, Pressure distribution on the frontal disk for turbulent flows in a radial diffuser, Exp. Therm. Fluid Sci. 60 (2015) 317–327. doi:10.1016/j.expthermflusci.2014.10.005.

[24] H.S. Ahn, G. Park, J.M. Kim, J. Kim, M.H. Kim, The effect of water absorption on critical heat flux enhancement during pool boiling, Exp. Therm. Fluid Sci. 42 (2012) 187–195. doi:10.1016/j.expthermflusci.2012.05.005.

[25] M.M. Rahman, E. Ölçeroglu, M. McCarthy, Role of wickability on the critical heat flux of structured superhydrophilic surfaces, Langmuir. 30 (2014) 11225–11234. doi:10.1021/la5030923.

[26] Z. Cao, B. Liu, C. Preger, Z. Wu, Y. Zhang, X. Wang, M.E. Messing, K. Deppert, J. Wei, B. Sundén, Pool boiling heat transfer of FC-72 on pin-fin silicon surfaces with nanoparticle deposition, Int. J. Heat Mass Transf. 126 (2018) 1019–1033. doi:10.1016/j.ijheatmasstransfer.2018.05.033.

[27] Z. Cao, Z. Wu, A.-D. Pham, Y. Yang, S. Abbood, P. Falkman, T. Ruzgas, C. Albèr, B. Sundén, Pool boiling of HFE-7200 on nanoparticle-coating surfaces: Experiments and heat transfer analysis, Int. J. Heat Mass Transf. 133 (2019) 548–560. doi:10.1016/j.ijheatmasstransfer.2018.12.140.

[28] Z. Wu, Z. Cao, B. Sundén, Saturated pool boiling heat transfer of acetone and HFE-7200 on modified surfaces by electrophoretic and electrochemical deposition, Appl. Energy. 249 (2019) 286–299. doi:10.1016/j.apenergy.2019.04.160.

[29] L. L. Manetti , T. S. Mogaji, P. A. Beck, E. M. Cardoso, Evaluation of the heat transfer enhancement during pool boiling using low concentrations of Al2O3 -water based nanofluid, Exp. Therm. Fluid Sci. 87 (2017) 191–200. doi:10.1016/j.expthermflusci.2017.04.018.

[30] I.S. Kiyomura, L.L. Manetti, A.P. da Cunha, G. Ribatski, E.M. Cardoso, An analysis of the effects of nanoparticles deposition on characteristics of the heating surface and ON pool boiling of water, Int. J. Heat Mass Transf. (2016). doi:10.1016/j.ijheatmasstransfer.2016.09.051.

[31] R.J. Moffat, Describing the Uncertainties in Experimental Results, (1988) 3–17.

[32] W. M. Rohsenow, A method of correlating heat transfer data for surface boiling of liquids. Transactions of ASME – J. Heat Transfer, Vol. 74, pp. 969-976 (1952).

[33] M.H. Rausch, L. Kretschmer, S. Will, A. Leipertz, A.P. Fröba, Density, surface tension, and kinematic viscosity of hydrofluoroethers HFE-7000, HFE-7100, HFE-7200, HFE-7300, and HFE-7500, J. Chem. Eng. Data. 60 (2015) 3759–3765. doi:10.1021/acs.jced.5b00691.

[34] I. S. Kiyomura , T. S. Mogaji, L. L. Manetti, E. M. Cardoso, A predictive model for confined and unconfined nucleate boiling heat transfer coefficient, Appl. Therm. Eng. 127 (2017) 1274–1284. doi:10.1016/j.applthermaleng.2017.08.135.

[35] Fritz, W. Berechnung des maximalvolumes von dampfblasen. Physik Zeitschr, Vol. 36, pp. 379-384 (1935).

[36] M.G. Cooper, Heat Flow Rates in Saturated Nucleate Pool Boiling-A Wide-Ranging Examination Using Reduced Properties, in: 1984: pp. 157–239. doi:10.1016/S0065-2717(08)70205-3.

[37] D. Gorenflo, Pool Boiling, VDI Heat Atlas. VDI-Verlag, Dusseldorf, Germany (1993).

[38] G. Ribatski, J.M.S. Jabardo, Experimental study of nucleate boiling of halocarbon refrigerants on cylindrical surfaces, Int. J. Heat Mass Transf. 46 (2003) 4439–4451. doi:10.1016/S0017-9310(03)00252-7.

[39] Stephan, K. Heat transfer in condensation and boiling: Springer-Verlag (1992).

[40] A. Priarone, Effect of surface orientation on nucleate boiling and critical heat flux of dielectric fluids, 44 (2005) 822–831. doi:10.1016/j.ijthermalsci.2005.02.014.

[41] V. V. Calmidi, R. L. Mahajan, The effective thermal conductivity of high porosity fibrous metal foams. Journal of Heat Transfer (1999). doi: 10.1115/1.2826001

[42] S. Mancin, C. Zilio, A. Diani, L. Rossetto. Air forced convection through metal foams: Experimental results and modeling. Int. J. Heat Mass Transf. 62 (2013), 112-123. doi: 10.1016/j.ijheatmasstransfer.2013.02.050

[43] S.J. Thiagarajan, R. Yang, C. King, S. Narumanchi, Bubble dynamics and nucleate pool boiling heat transfer on microporous copper surfaces, Int. J. Heat Mass Transf. 89 (2015) 1297–1315. doi:10.1016/j.ijheatmasstransfer.2015.06.013.

[44] Borishanskiy, A. V., Danilova, G. P., & Kupriyanova, A. V. Correlation of data on heat transfer in, and elementary characteristics of the nucleate boiling mechanism. Heat Transfer Sov. Res, Vol. 13, pp. 100-116 (1981).

[45] Phan, H. T., Caney, N., Marty, P., Colasson, S., & Gavillet, J. (2009). How does surface wettability influence nucleate boiling?. Comptes Rendus Mécanique, 337(5), 251-259. doi: 10.1016/j.crme.2009.06.032

[46] Cole, R., & Rohsenow, W. M. Correlation of bubble departure diameters for boiling of saturated liquids. In Chem. Eng. Prog. Symp. Ser, Vol. 65, pp. 211-213 (1968).

[47] A. K. Sadaghiani, A. R. Motezakker, S. Kasap, I. I. Kaya, A. Koşar, Foamlike 3D graphene coatings for cooling systems involving phase change. ACS Omega (2018), 2804-2811. doi: 10.1021/acsomega.7b02040

AUTHOR DECLARATION

1. Conflict of Interest

We wish to draw the attention of the Editor to the following facts, which may be considered as potential conflicts of interest, and to significant financial contributions to this work:

☒No conflict of interest exists.

We wish to confirm that there are no known conflicts of interest associated with this publication and there has been no significant financial support for this work that could have influenced its outcome.

2. Funding

☒Funding was received for this work.

All of the sources of funding for the work described in this publication are acknowledged in the manuscript file.

3. Intellectual Property

☒We confirm that we have given due consideration to the protection of intellectual property associated with this work and that there are no impediments to publication, including the timing of publication, with respect to intellectual property. In so doing we confirm that we have followed the regulations of our institutions concerning intellectual property.

4. Authorship

☒We confirm that the manuscript has been read and approved by all named authors.

☒We confirm that the order of authors listed in the manuscript has been approved by all named authors.

5. Contact with the Editorial Office

The Corresponding Author declared on the title page of the manuscript is:

POOL BOILING HEAT TRANSFER OF HFE-7100 ON METAL FOAMS

☒This author submitted this manuscript using his/her account in EVISE.

☒All authors understand that this Corresponding Author is the sole contact for the Editorial process (including EVISE and direct communications with the office). He/she is responsible for communicating with the other authors about progress, submissions of revisions and final approval of proofs.